R-matrix calculations of triplet gerade states of molecular hydrogen and their use for high-resolution spectroscopy

H. Oueslati,[1] F. Argoubi,[1] S. Bezzaouia,[1] M. Telmini,[1] and Ch. Jungen[2,3,*]

[1]*LSAMA Department of Physics, Faculty of Science of Tunis, University of Tunis El Manar, 2092 Tunis, Tunisia*

[2]*Laboratoire Aimé Cotton du CNRS, Université de Paris-Sud, 91405 Orsay, France*

[3]*Department of Physics and Astronomy, University College London, London WC1E 6BT, United Kingdom*

(Received 15 January 2014; published 4 March 2014)

A variational *R*-matrix approach combined with multichannel quantum defect theory is used for a computational study of triplet gerade states of H_2. Electron-ion reaction (quantum defect) matrices are calculated as functions of internuclear distance and energy for the bound and continuum ranges including singly and doubly excited configurations built on the $1\sigma_g$ ($X^+\,^2\Sigma_g{}^+$) and $1\sigma_u$ ($A^+\,^2\Sigma_u{}^+$) core states of the $H_2{}^+$ ion. It is shown how these matrices can be reduced to effective quantum defect functions adapted to the analysis of high-resolution spectra in the bound range. These *R*-matrix effective quantum defects are finally adjusted to the available experimental data [Sprecher *et al.*, J. Phys. Chem. A **117**, 9462 (2013)], producing agreement with experiment to within 0.5 cm^{-1}, nearly as good as obtained by Sprecher *et al*. In addition, the *R*-matrix calculations predict the evolution of the quantum defects for higher energies, in a range extending far into the electronic continuum.

DOI: 10.1103/PhysRevA.89.032501 PACS number(s): 31.15.vj, 32.80.Ee, 33.20.Wr, 34.50.Gb

I. INTRODUCTION

The *R*-matrix approach has been successfully applied to a wide range of atomic and molecular scattering problems [1]. Photoionization of complex atoms has been treated at a near-spectroscopic level [2], and in the case of electron-molecule collision problems the method has enabled large systems of biological interest to be treated in a meaningful way [3]. *R*-matrix calculations for small molecular systems have in some cases been extended into the bound range where the Rydberg manifolds occur [4–16]. The rotational, vibrational, and spin fine structures of molecular Rydberg states tend to form complex patterns due to the high density of rovibronic states close to the ionization threshold and due to strong nonadiabatic coupling between the electronic and nuclear degrees of freedom. For *ab initio* theory to be useful in this context, quite high accuracy is required. For instance, in order to obtain an accuracy of the order of a wave-number unit (cm^{-1}) for a state with a principal quantum number $n \approx 2$, the Rydberg electron phase shift or quantum defect must be evaluated correctly to within $\approx 10^{-5}$, an accuracy which probably has never been achieved in scattering calculations. Under favorable circumstances quantum chemistry is able to attain this level of accuracy: In the case of molecular hydrogen H_2 Wolniewicz and his collaborators have evaluated electronic energies for excited states $n \leqslant 5$ with sub-cm^{-1} precision [17]. As discussed in more detail in Sec. II below, *effective* phase shifts or quantum defects may be extracted from these accurate energies which turn out to be highly successful for the purposes of spectroscopic analysis which goes beyond the Born-Oppenheimer approximation [18]. However, this is in some sense an empirical approach, which leaves the question open of how exactly the accurate energies relate to a wave-function property, i.e., the electron phase shift. Moreover, traditional *ab initio* quantum chemistry is not able to maintain this sort of accuracy up to higher n members of molecular Rydberg series, not to speak of structures embedded in the electronic continua at higher energies.

In this paper we show with the example of the triplet gerade channels of H_2 how by starting out from first-principles *R*-matrix electron phase-shift matrix calculations, we can construct quantum defect matrices by successive transformations, which are directly applicable in the framework of multichannel quantum defect theory (MQDT) to the Rydberg spectroscopy of the triplet gerade states of H_2 ranging from $n = 2$–30 [19]. These transformations involve (i) the transformation from spheroidal to spherical quantum defects; (ii) the elimination of core-excited channels via application of physical boundary conditions to these; (iii) the parametrization in terms of analytic energy dependencies up to second order, separately for each bond length; and (iv) a final adjustment via a fit to experimental levels over a wide range of energies.

Three different units of energy are used in the various sections of this paper depending on whether the *ab initio* aspects of the calculation are discussed (Secs. II and III), or those dealing with quantum defect theory (Secs. IV and V), or high-resolution spectroscopy (Sec. V): These are, respectively, atomic units [a.u., $E/(\hbar^2/ma_0^2)$], "natural" Rydberg units [Ry, $E/(\hbar^2/2ma_0^2)$], and wave-number units (cm^{-1}, E/hc), where $a_0 = 4\pi\epsilon_0\hbar^2/me^2$ is the Bohr radius while the other symbols have their usual meaning.

II. EFFECTIVE QUANTUM DEFECTS EXTRACTED FROM CLAMPED-NUCLEI BORN-OPPENHEIMER CURVES

The left column of Fig. 1 depicts the existing quantum-chemical Born-Oppenheimer potential-energy curves of triplet gerade H_2 from the work of Wolniewicz, Kolos, and collaborators [17,20,21], along with the $1\sigma_g$ and $1\sigma_u$ ground-state and first excited-state curves of the ion core. These curves are accurate to less than 1 cm^{-1} or 10^{-5} a.u. and correspond to

[*]Visiting professor (2005–2006), Laboratorium für Physikalische Chemie, ETH-Zürich, 8093 Zürich, Switzerland.

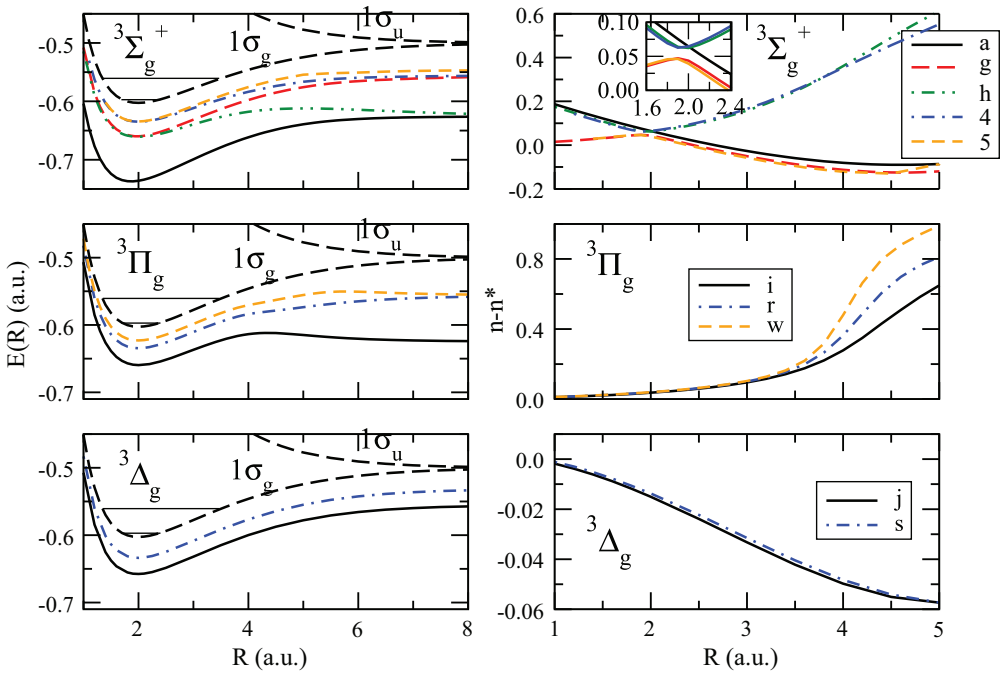

FIG. 1. (Color online) (Left column) Clamped-nuclei energies $E(R)$ as functions of the internuclear separation, R. Top to bottom: $^3\Sigma_g{}^+$ symmetry (a, g, h, 4, and 5 states), $^3\Pi_g$ symmetry (i, r, and w states), $^3\Delta_g$ symmetry (j and s states). The two long-dashed curves at the top in each panel represent the $1\sigma_g$ ($X^+\,{}^2\Sigma_g{}^+$) and $1\sigma_u$ ($A^+\,{}^2\Sigma_u{}^+$) ground and first-excited states of the ion core. The positions of the $v^+ = 0$ and 4 vibrational levels of the ion core ground state are indicated by horizontal thin lines. (Right column) (the color codings in the left and right columns are the same) Corresponding effective quantum defects $n - n^*$ evaluated with Eq. (1). The enlarged inset in the top-right panel illustrates the avoided crossing near $R = 2$ a.u. between $s\sigma$- and $d\sigma$-type effective quantum defect curves.

the present state of the art. A look at the left column of Fig. 1 immediately suggests—and this, of course, has been known for a long time [22]—that near equilibrium ($R \approx 2$) the curves form Rydberg series converging to the ion ground state. Thus, for $^3\Sigma_g{}^+$ we have a $ns\sigma$ series starting with $n = 2$ and a $nd\sigma$ series starting with $n = 3$. For $^3\Pi_g$ and $^3\Delta_g$ symmetry we have, respectively, $nd\pi$ and $nd\delta$ series starting with $n = 3$. Considering this zero-order one-electron picture, it is therefore tempting to extract "effective" quantum defects $\mu_n^{(\mathrm{eff})}$ using the Rydberg equation,

$$\mu_n^{(\mathrm{eff})}(R) = n - n^*(R) = n - \left\{2\left[E^+_{1\sigma_g}(R) - E_n(R)\right]\right\}^{-\frac{1}{2}}. \tag{1}$$

Here n and n^* are the principal (integer) and effective principal quantum number and E_n and E^+ are the molecular and ion clamped-nuclei energies in atomic units. The resulting effective quantum defects are plotted in the set of right-hand panels. At first sight the plots appear to demonstrate the physical reality of the simple one-electron picture in a striking manner.

(i) $^3\Delta_g$ symmetry: The quantum defect is small ($|\mu^{(\mathrm{eff})}| < 0.1$) and negative and varies little with R and n, in line with what is expected for a nonpenetrating $d\delta$ Rydberg electron.

(ii) $^3\Pi_g$ symmetry: The quantum defect increases monotonically with R and reaches values close to unity near $R = 5$ a.u. This behavior is characteristic for a "promoted" orbital $d\pi$ in the one-electron–two-center system (Mulliken [23]), i.e., one whose effective principal quantum number decreases by one unit upon dissociation and which therefore is antibonding. Equivalently, one may say that the quantum defect *increases* by one unit over the same range.

(iii) $^3\Sigma_g{}^+$ symmetry: Two distinct families of curves appear corresponding to a slightly bonding $s\sigma$ orbital (quantum defect monotonically decreasing with R) and a promoted antibonding $d\sigma$ orbital (quantum defect monotonically increasing with R).

While the effective quantum defect curves of Fig. 1 reveal the underlying one-electron Rydberg physics, they retain the high accuracy of the quantum-chemical calculations from which they have been derived via Eq. (1). However, the quantum-chemical calculations in turn are based on a sophisticated configuration interaction (CI) treatment, far beyond, and not invoking, the single-electron Rydberg picture. Indeed, these curves could not have been obtained in any meaningful way in a one-electron picture. This is demonstrated, for instance, by the work of Ref. [24], where quantum defect functions were computed for the singlet ungerade Rydberg states of H_2 based on Kohn's variational principle implemented in an independent-electron static-exchange approximation. Figures 5 and 6 of that reference show that these curves do not even qualitatively reproduce the exact values, both with regard to their values at equilibrium and to their evolution with R.

Signs of the breakdown of the single-electron Rydberg picture become apparent also in the present Fig. 1. An avoided crossing occurs between the $s\sigma$ and $d\sigma$ $^3\Sigma_g{}^+$ quantum defect functions near $R = 2$ a.u. for $n \geqslant 3$ (but not for $n = 2$ since no $2d\sigma$ state exists) and reveals the presence of nonspherical ℓ-mixing interactions even at small internuclear distances.

Strong n dependencies of the $^3\Sigma_g{}^+$ and $^3\Pi_g$ quantum defect functions appear for $R \geqslant 4$ a.u. in Fig. 1 and indicate the presence of increasingly strong configuration mixing (CM). Indeed, as the internuclear separation becomes larger, "major CM"—in terms of Mulliken's [25] concepts—sets in and eventually leads to a new regime where it is dominant and the independent-electron approximation breaks down because the one-electron states are now "entangled." We conclude that the plots displayed on the right column of Fig. 1 convey a deceivingly simplified picture which provides physical insight but cannot be used for quantitative predictions. The goal of the present paper is to define a procedure that fills the gap between the intuitive and the quantitative approaches.

III. R-MATRIX CALCULATIONS OF TRIPLET GERADE QUANTUM DEFECTS OF H_2

A. Variational R-matrix approach

In recent years we have developed an *ab initio* R-matrix approach [15] which enables bound states and core-excited scattering states of H_2 to be calculated for fixed nuclei. Our work is based on the ideas of Greene and Yoo [11], which it adapts such as to yield quantum defect matrices that evolve smoothly throughout the bound and continuous energy regions, and which also vary reasonably mildly as functions of the molecular geometry (internuclear distance R). Our "halfium model" combines the variational eigenchannel R-matrix method [26] with the generalized multichannel quantum defect theory (GMQDT) [27] implemented using prolate spheroidal electron coordinates. The approach has been used to investigate singlet ungerade symmetries ($^1\Sigma_u$, $^1\Pi_u$) [15,28] and gerade symmetries ($^1\Sigma_g$, $^1\Pi_g$, $^1\Delta_g$) [16] of H_2, both for the bound and the continuum (autoionization) regions as well as for very highly excited states of Σ^- symmetry [29,30].

The R-matrix method is not particularly adapted *a priori* to treat systems for very large internuclear distances, and up to date most applications have dealt with molecules at or near their equilibrium geometries [3]. However, owing to the use of spheroidal coordinates the halfium model appears well adapted to be applied for moderately large R values. Its implementation in terms of these coordinates allows the partial wave expansion of the electron wave functions to be kept to a minimum. The R-matrix scheme leads to a global analysis of the interactions as no distinction is made between "open" and "closed" channels at the outset, but instead all channels are treated on the same footing irrespective of their channel thresholds. In this picture core-excited states are included explicitly as electron-ion collision channels in their own right.

In the halfium model, the two-electron configuration space is divided into two regions: (i) a reaction volume where the variational R-matrix method is employed and (ii) the remaining space, called the asymptotic zone, where GMQDT is used. The connection of the inner-zone and outer-zone wave functions then yields the desired reaction matrix or equivalent quantum defect matrix. In the inner zone the full nonrelativistic two-electron Hamiltonian is taken into account, whereas in the asymptotic zone the single escaping electron is assumed to move in the field of two $Z = \frac{1}{2}$ point charges separated by R, with polarization terms added on each center following the method of Ref. [13]. This halfium representation of the asymptotic field representation is more realistic than the spherical Coulomb field with $Z = 1$, which is commonly used in R-matrix calculations, as the half charges provide a reasonable approximation to the nonspherical field of the ion core and in particular to its quadrupole component [31].

Each two-electron basis function defined in the reaction zone is expressed in spheroidal coordinates (ξ,η,φ) and corresponds to a configuration i,j (cf. [15,29]) with a specified set of quantum numbers $\{S,\Lambda,p,q\}$ and including appropriate symmetrization. The reaction zone is defined by a preselected value ξ_0 which typically varies with the molecular geometry, R. S and Λ refer to the total electron spin and the component of orbital angular momentum along the molecular axis as usual, while the indices p and q refer, respectively, to the symmetry gerade or ungerade [$(-1)^p$ with p *even* or *odd*] and to $-$ symmetry ($q = 1$) or $+$ symmetry ($q = 0$) depending on whether the sign changes or not upon reflection σ_v of all electron coordinates at any plane containing the two nuclei. Two of these four quantum numbers, S and q, appear explicitly in the wave-function expressions given below, while the other two, Λ and p, impose requirements on the selection of molecular orbitals, as detailed below.

For $\Lambda = 0$ we write

$$\overline{y}_{ij}(\vec{r_1},\vec{r_2}) = \overline{N}_{ij}[y_{ij}^{+-}(\vec{r_1},\vec{r_2}) + (-1)^q\, y_{ij}^{-+}(\vec{r_1},\vec{r_2})], \quad (2)$$

where $\vec{r_1}$ and $\vec{r_2}$ are the position vectors of each electron defining the corresponding spheroidal coordinates (ξ,η,φ). The functions y_{ij}^{+-} and y_{ij}^{-+} are products of one-electron orbitals characterized by signed orbital angular momentum components,

$$\begin{aligned} y_{ij}^{+-}(\vec{r_1},\vec{r_2}) &= N_{ij}[\phi_i^+(\vec{r_1})\phi_j^-(\vec{r_2}) + (-1)^S\phi_j^-(\vec{r_1})\phi_i^+(\vec{r_2})], \\ y_{ij}^{-+}(\vec{r_1},\vec{r_2}) &= N_{ij}[\phi_i^-(\vec{r_1})\phi_j^+(\vec{r_2}) + (-1)^S\phi_j^+(\vec{r_1})\phi_i^-(\vec{r_2})], \end{aligned} \quad (3)$$

with

$$\begin{aligned} \phi_i^{\pm}(\vec{r}) &= \frac{\chi_i(\xi)}{\sqrt{\xi^2-1}}\frac{\zeta_i(\eta)}{\sqrt{1-\eta^2}}\frac{1}{\sqrt{2\pi}}\exp(\pm i\lambda_i\varphi) \\ &\equiv \frac{\chi_i(\xi)}{\sqrt{\xi^2-1}}Y_{\tilde{\ell}_i,\pm\lambda_i}(\eta,\varphi), \end{aligned} \quad (4)$$

the ith $H_2{}^+$ one-electron wave function confined to the reaction volume. For $\Lambda = 0$, $\lambda_i = \lambda_j$ is selected (where $\lambda \geqslant 0$ is assumed). For $\Lambda \neq 0$ the condition $\lambda_i = \lambda_j$ is relaxed, and functions y_{ij}^{++} and y_{ij}^{--} are also used in Eqs. (2) and (3) when $\Lambda > 0$ is even, corresponding to $|\Lambda| = |\lambda_i + \lambda_j|$. N_{ij} and $\overline{N}_{ij}$ are normalization factors given in Ref. [29].

Each one-electron function defined by Eq. (4) may be designated by the shorthand ket notation $|i\rangle = |n_i\tilde{\ell}_i\lambda_i\rangle$. It is implied here and later in this section that $\tilde{\ell}_i$ is the generalized orbital angular momentum quantum number arising when spheroidal coordinates are used [15]. The factors $Y_{\tilde{\ell}\lambda}(\eta,\varphi)$ on the second line of Eq. (4) thus are normalized spheroidal harmonics, analogous to the familiar spherical harmonics (see [13] for the definitions and numerical implementation that

we use). The one-electron functions $|i\rangle$ are therefore gerade when $\tilde{\ell}$ is even, and they are ungerade when $\tilde{\ell}$ odd. The desired symmetry g/u of the two-electron functions is then $(-1)^p = (-1)^{\tilde{\ell}_i+\tilde{\ell}_j}$ and is obtained by appropriately combining even and/or odd $\tilde{\ell}$ orbitals. The basis of two-electron functions $\overline{y}_{ij}$ used in the variational R-matrix approach consists both of "closed" functions whose radial component $\chi^{(c)}(\xi_0)$ in Eq. (4) vanishes on the reaction surface $\max(\xi_1,\xi_2) = \xi_0$ and of "open" functions whose radial component $\chi^{(o)}(\xi_0)$ is nonzero but has a vanishing radial derivative on the reaction surface $\max(\xi_1,\xi_2) = \xi_0$ [11,15].

The two-electron basis functions are used to solve the Schrödinger equation inside the reaction volume in the way prescribed by the variational R-matrix method for any given total energy E. The eigensolutions are denoted $\overline{\Psi}_\beta(\vec{r_1},\vec{r_2})$, where β is a solution index, and are characterized by stationary logarithmic derivatives b_β on the reaction surface $\max(\xi_1,\xi_2) = \xi_0$. They are obtained inside the reaction volume as an expansion over the two-electron configurations,

$$\overline{\Psi}_\beta = \sum_{ij} c_{ij}^{(\beta)} \overline{y}_{ij}, \tag{5}$$

where the expansion coefficients $c_{ij}^{(\beta)}$ are the result of the variational calculation.

Each solution $\overline{\Psi}_\beta$ may be continued in the external zone, i.e., for radii of the outer electron larger than ξ_0, as a linear combination of regular and irregular two-center Coulomb radial functions,

$$\overline{\Psi}_\beta(E,\omega,\xi \geqslant \xi_0) = \sum_k \overline{\Phi}_k(E,\omega) \frac{1}{\sqrt{\xi^2-1}} \times [f_k(\epsilon_k,\xi) I_{k\beta}(E) - g_k(\epsilon_k,\xi) J_{k\beta}(E)]. \tag{6}$$

Here E is the total energy and $\epsilon_k = E - E_k^+$ is the energy of the outer electron with respect to the state E_k^+ of the residual core corresponding to the channel k and for the given R value. ω stands for all coordinates except the radial coordinate of the outermost electron. The summation index k runs over those channels $k \equiv i'j'$, which are taken into account explicitly in the asymptotic zone. The matching of the outer and inner eigensolutions defines the coefficient matrix elements $I_{k\beta}$ and $J_{k\beta}$ that appear on the right-hand side of Eq. (6). This equation also shows how the matching requires expanding each inner-zone variational solution Ψ_β on the reaction surface in terms of so-called "surface harmonics," $\overline{\Phi}_k(\omega)$, for each asymptotic channel k and for each solution β (see [15]). The form of these surface harmonics as well as their symmetrization and normalization is detailed in Ref. [29].

By projecting each R-matrix eigensolution $\overline{\Psi}_\beta(\vec{r_1},\vec{r_2})$ onto a surface harmonic $\overline{\Phi}_k(\omega)$ at $\max(\xi_1,\xi_2) = \xi_0$, one obtains surface expansion coefficients $\overline{u}_{k\beta}(\xi_0)$ of the form

$$\overline{u}_{k\beta}(\xi_0) = \langle\langle \overline{\Phi}_k(\omega) | \overline{\Psi}_\beta(\omega,\xi_0) \rangle\rangle = f_k(\xi_0) I_{k\beta} - g_k(\xi_0) J_{k\beta} \tag{7}$$

(where the energy dependencies have been omitted for clarity). The detailed expression of the projection integral $\langle\langle \cdots \rangle\rangle$ (integration over ω) is given in Ref. [29]. In order to ensure the continuity of the wave function as well as of its derivative across the reaction surface, the projection integrals $\overline{u}_{k\beta}$ must also satisfy the equation

$$b_\beta \overline{u}_{k\beta}(\xi_0) = f_k'(\xi_0) I_{k\beta} - g_k'(\xi_0) J_{k\beta}, \tag{8}$$

where b_β is the logarithmic derivative for each variational solution β obtained in constructing the expansion Eq. (5) and the primes refer to the radial derivative.

By combining the matching conditions, Eqs. (7) and (8), the matrices $\mathbf{I}$ and $\mathbf{J}$ and hence the short-range reaction matrix $\mathbf{K} = \mathbf{J}\mathbf{I}^{-1}$ and equivalent quantum defect matrix are determined.

B. Multicore-multichannel R-matrix quantum defects

In order to test the robustness and power of the R-matrix approach, we have deliberately carried out the calculations reported here with minimal basis sets, both with regard to the radial and angular components included, as well as with regard to the electronic ion core (target) states retained in the calculations. We explicitly included only the $1\sigma_g$ and $1\sigma_u$ core states in the asymptotic region ($\xi \geqslant \xi_0$) and we limited the partial wave expansion to $\tilde{\ell} \leqslant 3$. This scheme leads to the following triplet gerade channels to be considered:

$$\begin{aligned} {}^3\Sigma_g^+ &: (1\sigma_g)\epsilon\tilde{s}\sigma, \quad (1\sigma_g)\epsilon\tilde{d}\sigma, \quad (1\sigma_u)\epsilon\tilde{p}\sigma, (1\sigma_u)\epsilon\tilde{f}\sigma, \\ {}^3\Pi_g &: (1\sigma_g)\epsilon\tilde{d}\pi, \quad (1\sigma_u)\epsilon\tilde{p}\pi, \quad (1\sigma_u)\epsilon\tilde{f}\pi, \\ {}^3\Delta_g &: (1\sigma_g)\epsilon\tilde{d}\delta, \quad (1\sigma_u)\epsilon\tilde{f}\delta. \end{aligned} \tag{9}$$

The angular basis used in the inner R-matrix region was also restricted to $\tilde{\ell} \leqslant 3$. For each angular component ten radial basis functions $\chi(\xi)$ [Eq. (4)] were evaluated, of which eight were closed and two were open (i.e., whose radial component or radial derivative, respectively, vanishes on the reaction surface). The number of antisymmetrized configurations $\bar{y}_{ij}$ [Eq. (2)] then ranged from 50 to 200 depending on the symmetry and the R value considered. Details concerning the selection of configurations may be found in Ref. [15].

The R-matrix procedure is adapted to situations where only one of the electrons at a time effectively escapes from the core. This means that the reaction volume defined by ξ_0 should be chosen large enough that the $n = 1$ H_2^+ orbitals are enclosed within the ellipsoid of revolution and become identical to the corresponding quantum-chemical H_2^+ orbitals in the usual sense. We have chosen ξ_0 as small as possible, in such a way that the energies of the enclosed $1\sigma_u$ orbital and the quantum-chemical one differ by less than about 0.001 a.u. Note, however, that in the MQDT calculations we use the exact values of the H_2^+ threshold energies. The values of ξ_0 adopted vary from 11 to 4 over the range $R = 1.4$ to 5.0 bohr. The value of the major axis of the ellipsoid varies from 7.70 to 10.00 bohr over the same range, while the minor axis varies from 7.67 to 9.68 bohr, indicating that the ellipsoids used in this R range deviate only slightly from spheres. The calculations have been carried out from $R = 1.4$ to 5.0 bohr with a grid spacing of 0.2 bohr. Typically about 20 calculations were carried out per R value, spanning the energy range from $\epsilon = -0.2$ to $+0.1$ a.u. with respect to the $1\sigma_g$ threshold.

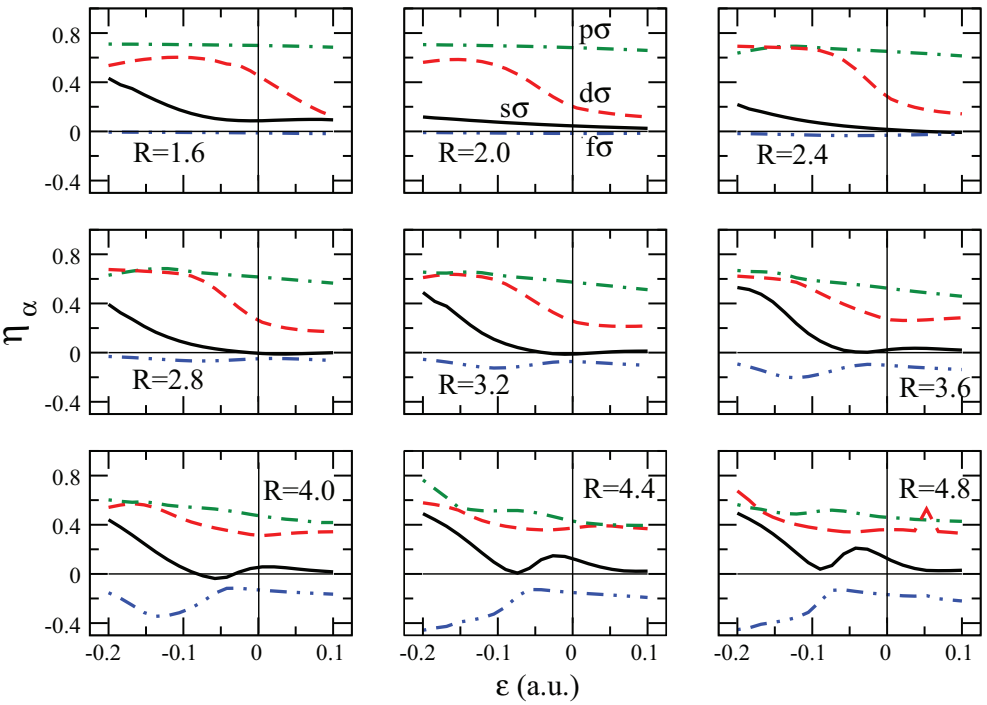

FIG. 2. (Color online) Spherical eigenquantum defects (η defects) for $^3\Sigma_g{}^+$ symmetry channels in H_2, plotted as functions of the electron energy $\epsilon = E - E^+(1\sigma_g)$ in a.u. Different panels correspond to different values of the internuclear distance R as indicated. For $R = 2.0$ a.u. and $\epsilon \approx 0$ the dominant contribution to each of the four eigenchannels is as follows: $(1\sigma_g)\epsilon\tilde{s}\sigma$, full line (black online); $(1\sigma_g)\epsilon\tilde{d}\sigma$, dashed line (red online); $(1\sigma_u)\epsilon\tilde{p}\sigma$, dot-dashed line (green online); $(1\sigma_u)\epsilon\tilde{f}\sigma$, dot-dot-dashed line (blue online).

IV. REDUCTION TO EFFECTIVE SPHERICAL SINGLE-CORE–MULTICHANNEL QUANTUM DEFECTS

A. Transformation from spheroidal to spherical coordinates

In order to construct spherical quantum defect matrices we return to the R-matrix solutions $\bar{\Psi}_\beta$ of Eq. (6) and their spheroidal asymptotic form given there. Equation (6) is valid for any $\xi \geqslant \xi_0$ with the coefficients $I_{k\beta}$ and $J_{k\beta}$ determined for $\xi = \xi_0$. We now use Eq. (6) to evaluate the R-matrix eigensolutions on a sphere $r = r_0$, centered on the midpoint between the nuclei. r_0 is chosen such that it encloses the ellipsoid defined by ξ_0. Then the matching procedure [Eqs. (7) and (8)], is repeated with the difference that the asymptotic channel functions in the summation of Eq. (6) are now

$$\Psi_\beta(E,\omega,r) = \sum_k \phi_c(\xi_1,\eta_1,\varphi_1) Y_{\ell\lambda}(\theta,\phi)\frac{1}{r} \times \left[f_k^{(\mathrm{sph})}(\epsilon_k,r) I_{k\beta}^{(\mathrm{sph})} - g_k^{(\mathrm{sph})}(\epsilon_k,r) J_{k\beta}^{(\mathrm{sph})}\right], \quad (10)$$

where ϕ_c is the core wave function, still represented in spheroidal coordinates, while $Y_{\ell\lambda}$ are ordinary spherical harmonics and $f_k^{(\mathrm{sph})}$ and $g_k^{(\mathrm{sph})}$ are Ham's radial functions as defined by Seaton [32] (his "nearly analytic" functions f and h). The relation

$$K_{kk'}^{(\mathrm{sph})} \equiv \tan \pi \eta_{kk'} = \sum_\beta J_{k\beta}^{(\mathrm{sph})} [I^{(\mathrm{sph})}]^{-1}_{\beta k'} \quad (11)$$

now yields *spherical* quantum defect matrices $\eta_{kk'}$ of the Ham type [32]—so-called η defects—which are appropriate for use in the framework of the customary quantum defect combined with frame transformation theory. Our $\mathbf{K}^{(\mathrm{sph})}$ corresponds to $\mathbf{Y}$ in Seaton's notation [32].

The results of the variational calculations are illustrated by Figs. 2–4 for $^3\Sigma_g{}^+$, $^3\Pi_g$, and $^3\Delta_g$ symmetry, respectively. The quantities plotted in the figures are the eigenquantum defects defined as

$$\eta_\alpha(E) = \frac{1}{\pi}\tan^{-1}\sum_{kk'} U_{\alpha k}^T(E) K_{kk'}^{(\mathrm{sph})}(E) U_{k'\alpha}(E), \quad (12)$$

where $\mathbf{U}$ is the eigenvector matrix of the reaction matrix $\mathbf{K}^{(\mathrm{sph})}$ from Eq. (11). The evolution of the η_α as function of the energy is displayed for selected R values. The curves provide an overview of the channel interactions over a range of energies that extends from strongly bound electronic states through the $1\sigma_g$ threshold up into the ionization continuum. It may be seen that the quantum defects evolve substantially with energy and internuclear separation in the ranges shown, but these evolutions are smooth rather than erratic. In particular, the quantum defects exhibit a continuous variation across threshold, demonstrating the basic physical continuity that links the discrete range to the ionization continuum.

B. Elimination of core-excited channels

In this work we are primarily interested in bound or quasibound molecular Rydberg states. The reaction matrices $\mathbf{K}$ produced by the R-matrix calculation may be used to evaluate clamped-nuclei energies equivalent to (but of course less accurate than) those obtained by state-of-the-art quantum chemistry. To this end we must apply the *physical* boundary conditions to the multichannel radial wave

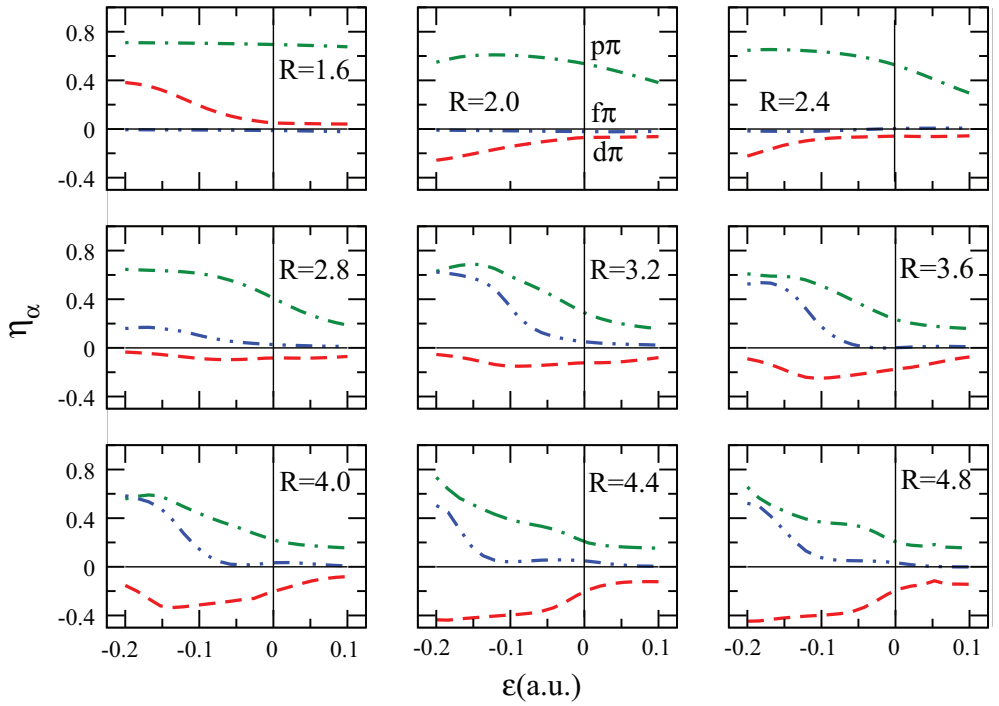

FIG. 3. (Color online) Spherical eigenquantum defects (η defects) for $^3\Pi_g$ symmetry channels in H_2, plotted as functions of the electron energy $\epsilon = E - E^+(1\sigma_g)$ in a.u. Different panels correspond to different values of the internuclear distance R as indicated. For $R = 2.0$ a.u. and $\epsilon \approx 0$ the dominant contribution to each of the three eigenchannels is as follows: $(1\sigma_g)\epsilon\tilde{d}\pi$, dashed line (red online); $(1\sigma_u)\epsilon\tilde{p}\pi$, dot-dashed line (green online); $(1\sigma_u)\epsilon\tilde{f}\pi$, dot-dot-dashed line (blue online).

functions, specifically in the bound range all components of the electronic wave function must vanish at infinity. This procedure has been followed in Refs. [15,16] for the singlet ungerade and gerade states. The secular equation

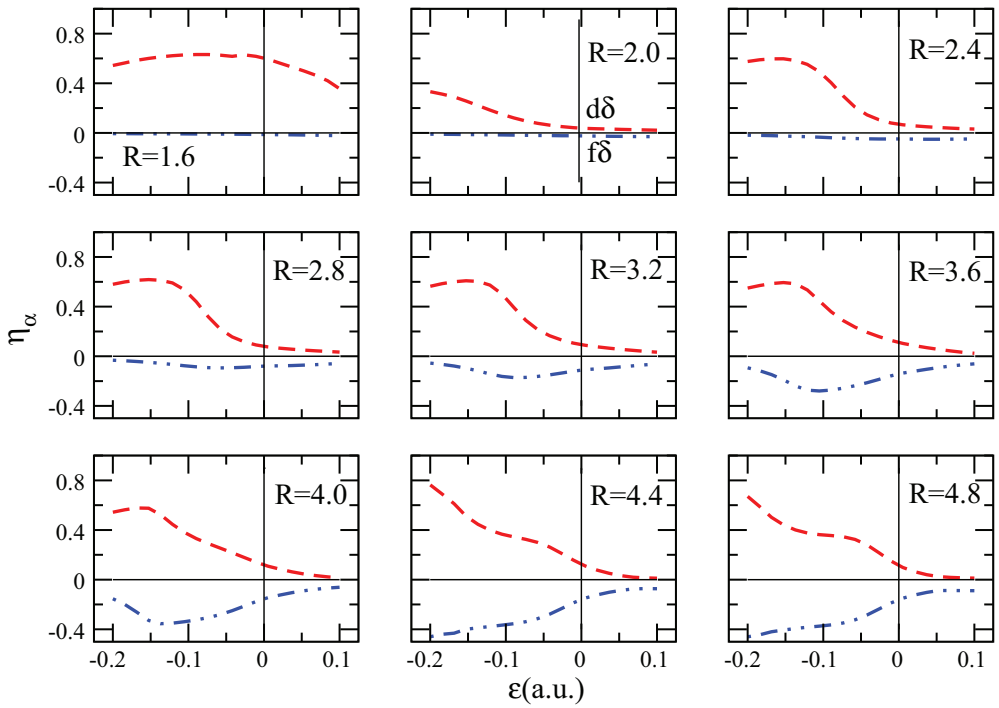

FIG. 4. (Color online) Spherical eigenquantum defects (η defects) for $^3\Delta_g$ symmetry channels in H_2, plotted as functions of the electron energy $\epsilon = E - E^+(1\sigma_g)$ in a.u. Different panels correspond to different values of the internuclear distance R as indicated. For $R = 2.0$ a.u. and $\epsilon \approx 0$ the dominant contribution to each of the two eigenchannels is as follows: $(1\sigma_g)\epsilon\tilde{d}\delta$, dashed line (red online); $(1\sigma_u)\epsilon\tilde{f}\delta$, dot-dot-dashed line (blue online).

of MQDT,

$$\det\left|\tan\beta_k(\epsilon_k)\delta_{kk'} + K^{(\mathrm{sph})}_{kk'}(E)\right| = 0, \tag{13}$$

is solved separately for each R value and total energy E and yields discrete electronic eigenenergies $E_n(R)$ which are converted into potential energy curves by adding the internuclear repulsion energy. β_k in Eq. (13) is the accumulated phase of the external electron in channel k, characterized by the channel energy $\epsilon_k = E - E_k^+$, where E_k^+ is the core energy as before. In the one-center Coulombic problem at hand the quantity $\beta_k/\pi + \ell$ is simply the familiar Rydberg effective principal quantum number $\nu_k = (-\epsilon_k)^{-1/2}$ (where ϵ_k is in Rydbergs) equivalent to n^* in Eq. (1). When η defects are used such as here, one has to set

$$\tan\beta_k(\epsilon_k) = \frac{\tan\pi\nu_k}{A(\epsilon_k,\ell_k)}, \tag{14}$$

where A is Ham's scaling factor [32].

Here, instead, we seek to evaluate smooth quantum defect curves such as those displayed in Figs. 2–4, but where the core-excited channels have been "eliminated" and their effect incorporated into the effective ground-state core quantum defects. We achieve this by applying the physical boundary condition Eq. (14) to the core-excited channels *only*, while treating the channels associated with the ground-state core artificially as *open* regardless of the sign of the corresponding ϵ. In practice, this means that for these latter channels the accumulated radial phase β_k in Eq. (13) is simply replaced by $-\pi\eta^{(\mathrm{red})}$. Equation (13) then yields the *reduced* eigenquantum defects $\eta_\alpha^{(\mathrm{red})}$ as functions of the continuous energy variable E, where α is a solution index. This type of MQDT procedures is explained in detail, e.g., in Refs. [33] or [34]. In the course of this operation the number of channels is *reduced* from 4 to 2, 3 to 1, and 2 to 1, respectively, for the $^3\Sigma_g{}^+$, $^3\Pi_g$, and $^3\Delta_g$ symmetries [cf. Eq. (9)]. Their number corresponds now to the sets of effective quantum defect curves shown in the right column of Fig. 1. The reduced eigenquantum defects $\eta_\alpha^{(\mathrm{red})}$ along with the eigenvector matrices $\mathbf{U}^{(\mathrm{red})}$ define the reduced spherical reaction matrices $\mathbf{K}^{(\mathrm{sph,red})}$. In the following we always refer to the reduced spherical matrices unless explicitly indicated, and therefore we drop the corresponding superscripts. At the same time the channel index k now coincides with the partial wave component ℓ of the outer electron associated with the ground-state core and is denoted accordingly [see Eq. (9)].

A further subtlety involves the following. As in previous work [35]—and justified there—we have found it advantageous to determine quantum defect matrix elements $\bar\eta_{\ell\ell'}$ instead of the usual $\eta_{\ell\ell'}$. The latter are related to the reaction matrix $\mathbf{K}$ as usual by $K_{\ell\ell'} = \tan\pi\eta_{\ell\ell'}$ (with the tangent taken element by element), while the former are related to the latter by

$$\bar\eta_{\ell\ell'} = (\pi^{-1})\mathbf{U}\arctan[\mathbf{U}^T\tan\pi\eta_{\ell\ell'}\mathbf{U}]\mathbf{U}^T, \tag{15}$$

where $\mathbf{U}$ is the (unitary) eigenvector matrix of $\mathbf{K}$.

The reduced $\bar\eta$ quantum defect matrix elements thus obtained are plotted in Figs. 5 and 6 as functions of the energy for various values of R as indicated. They are seen to exhibit smooth energy dependencies in the bound range, but develop a resonant behavior at higher energies. The resonances are due the $\ell = 1$ and 3 Rydberg series associated according to

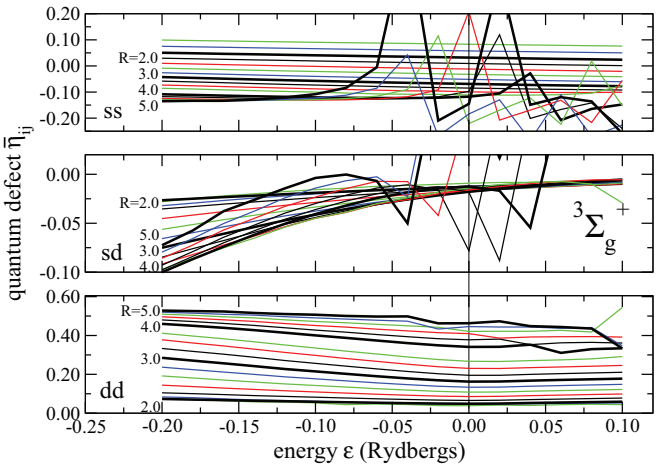

FIG. 5. (Color online) Reduced spherical quantum defect matrix elements $\bar\eta_{ss}$, $\bar\eta_{sd}$, and $\bar\eta_{dd}$ for $^3\Sigma_g{}^+$ symmetry channels in H_2, obtained by elimination of the closed core-excited $(1\sigma_u)\epsilon p\sigma$ and $(1\sigma_u)\epsilon f\sigma$ channels. The defects are plotted as functions of the electron energy $\epsilon = E - E^+(1\sigma_g)$ in Rydbergs. Thick lines (black online) correspond to $R = 2$, 3, 4, and 5 bohr, respectively, as indicated. Thin lines (color coded online) represent intermediate R values with increments of 0.2 bohr.

Eq. (9) with the $1\sigma_u$ excited core, which now appear because the physical boundary conditions have been applied to the core-excited channels. The zigzag patterns seen in Figs. 5 and 6 are due to the fact that we use a coarse energy grid in our calculations. On a fine grid the full pole-type structure would emerge. However, the purpose here is not to study those resonances in detail: It is indeed their *absence* that determines

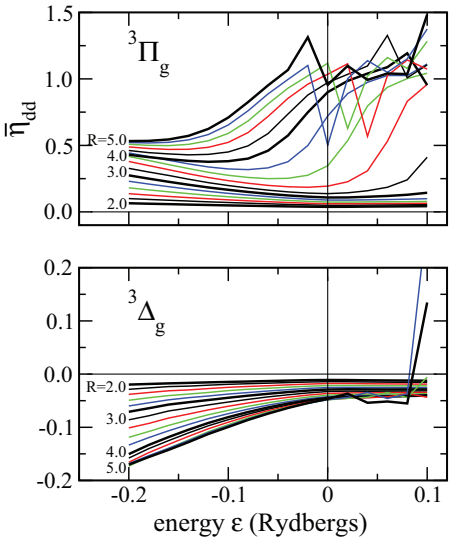

FIG. 6. (Color online) Reduced spherical quantum defect matrix elements $\bar\eta_{dd}$ for $^3\Pi_g$ (top panel) and $^3\Delta_g$ (bottom panel) symmetry channels in H_2, obtained by elimination of the closed core-excited $(1\sigma_u)\epsilon p\pi$ and $(1\sigma_u)\epsilon f\pi$ $(\epsilon f\delta)$ channels. The defects are plotted as functions of the electron energy $\epsilon = E - E^+(1\sigma_g)$ in Rydbergs. Thick lines (black online) correspond to $R = 2$, 3, 4, and 5 bohr, respectively, as indicated. Thin lines (color coded online) represent intermediate R values with increments of 0.2 bohr.

how far the reduced quantum defect matrices remain smooth and retain their usefulness. It may be seen that the $^3\Sigma_g{}^+$ channels are most strongly perturbed, with the resonance patterns setting in below threshold, whereas the $^3\Delta_g$ channels are least perturbed and the resonance pattern sets in above threshold. Further, it appears clearly that the larger R, the earlier occurs the onset of the resonances, a fact which is not surprising in view of the repulsive character of the $1\sigma_u$ ion core state which comes down as R increases, see the left column of Fig. 1.

C. Explicit energy dependencies

The results displayed in Figs. 5 and 6 are intended for use in the bound range, i.e., $\epsilon < 0$, in the framework of rovibronic molecular MQDT. To this end it is convenient to represent the smooth portion of each quantum defect matrix element by an expansion in energy around $\epsilon = 0$,

$$\bar{\eta}_{\ell\ell'}(\epsilon,R) = \bar{\eta}_{\ell\ell'}(R) + \frac{\partial\bar{\eta}_{\ell\ell'}(R)}{\partial\epsilon}\epsilon + \frac{1}{2}\frac{\partial^2\bar{\eta}_{\ell\ell'}(R)}{\partial\epsilon^2}\epsilon^2 + \cdots$$
$$\equiv \bar{\eta}^{(0)}(R) + \bar{\eta}^{(1)}(R)\epsilon + \frac{1}{2}\bar{\eta}^{(2)}(R)\epsilon^2 + \cdots . \quad (16)$$

In practice, we retain only terms up to second order. Figures 7 and 8 display the result of this procedure (black circles). These curves contain the first-principles dynamical information on channel couplings in the triplet gerade Rydberg manifolds of H_2 in condensed form. They are designed for use in a rovibronic quantum defect treatment that involves only the ground-state ion explicitly, but implicitly takes account of the effects of CIs involving core-excited channels. Figures 5 and 6 allow one to assess over which range of energy ϵ and internuclear separation R the expansion Eq. (16) remains meaningful.

Finally, since the *ab initio* R-matrix points of Figs. 7 and 8 exhibit some slight scatter (e.g., the values for $R = 3.8$ a.u. for $^3\Sigma_g{}^+$ symmetry), we have subjected them to a smoothing procedure by fitting their R dependence to polynomials of order 4 to 6, as appropriate for each curve. These smoothened curves are represented by full lines (red online) and contain the final R-matrix information that we combine below with standard MQDT techniques to calculate the rovibronic fine structure of the triplet gerade channels in H_2. A last step, described in Sec. V, involves adjusting the curves by fitting them to experimental data in order to achieve spectroscopic accuracy.

V. REFINEMENT OF THE QUANTUM DEFECTS BY FITTING TO EXPERIMENTAL ENERGY LEVELS

A. Rovibronic MQDT and frame transformation

In order to calculate the rovibronic structure of the triplet gerade Rydberg states in the framework of MQDT we must solve the MQDT determinantal system Eq. (13) once again, but now by taking account of rovibrational motion. First, the phase parameters $\beta_k(\epsilon) \equiv \beta_\ell(\epsilon)$ in Eqs. (13) and (14), instead of being taken with ϵ for any fixed R value, must now be taken with respect to the rovibrational thresholds of the $X\,^2\Sigma_g{}^+$ ion ground state. One therefore uses $\epsilon_{v^+N^+} = E - E^+_{v^+N^+}$, where the quantum numbers v^+ and N^+ refer to the vibrating and rotating ion core. Second, the clamped-nuclei reaction matrix elements $K^{(\mathrm{sph})}_{\ell\ell'}(E,R)$ of Eq. (13) are replaced by rovibronic reaction matrix elements $K^{(\mathrm{sph})(N,p)}_{\ell v^+N^+,\ell' v^{+'}N^{+'}}(E)$, with $p = 0$ or 1

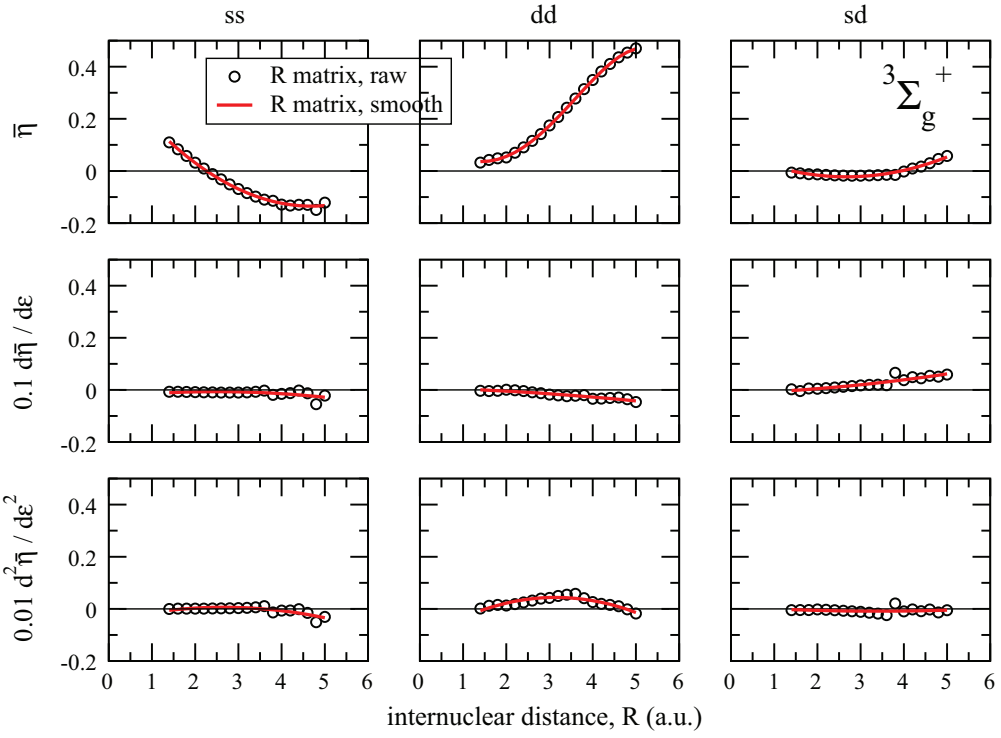

FIG. 7. (Color online) Energy dependencies of $\bar{\eta}_{ss}$, $\bar{\eta}_{dd}$ $\bar{\eta}_{sd}$ quantum defects for $^3\Sigma_g{}^+$ symmetry channels in H_2 at $\epsilon = 0$, plotted as functions of the internuclear distance R. (Top row) $\bar{\eta}_{ij}$; (middle row) $0.1 \times \partial\bar{\eta}/\partial\epsilon$; (bottom row) $0.01 \times \partial^2\bar{\eta}/\partial\epsilon^2$. Circles, raw R-matrix values; full lines (red online), smoothened R-matrix values. Energies are in Rydbergs.

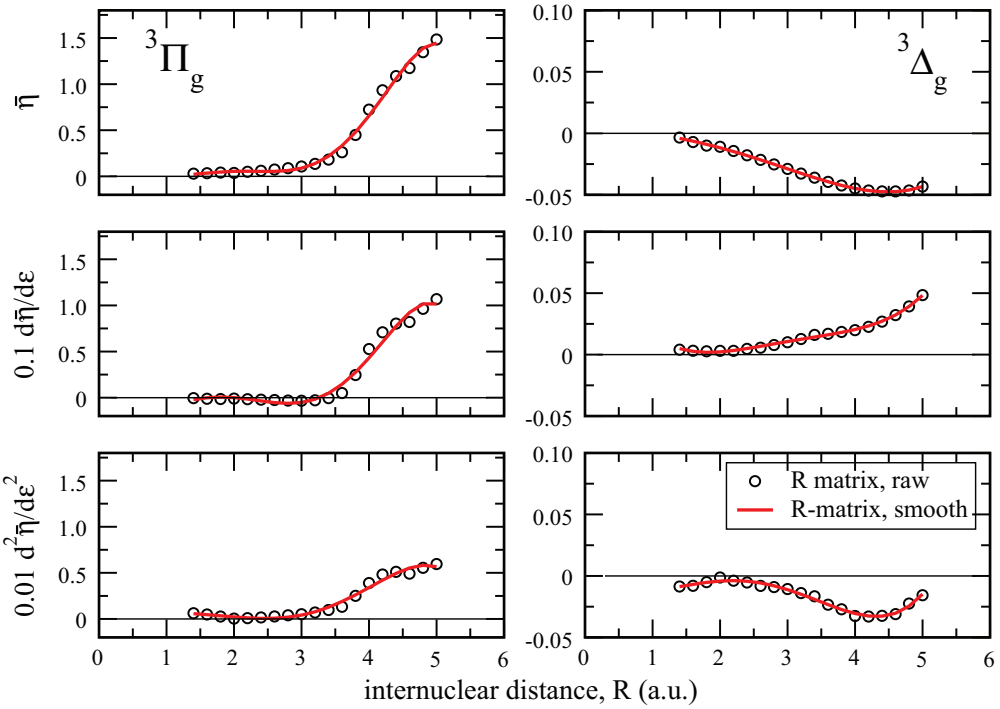

FIG. 8. (Color online) Energy dependencies of $\bar{\eta}_{dd}$ quantum defects for $^3\Pi_g$ (left) and $^3\Delta_g$ (right) symmetry channels in H_2 at $\epsilon = 0$, plotted as functions of the internuclear distance R. (Top row) $\bar{\eta}_{ij}$; (middle row) $0.1 \times \partial\bar{\eta}/\partial\epsilon$; (bottom row) $0.01 \times \partial^2\bar{\eta}/\partial\epsilon^2$. Full lines (red online), smoothened R-matrix values. Energies are in Rydbergs.

referring to the total parity $(-1)^p$ of the rovibronic channel (not to be confused with the purely electronic index p introduced in Sec. III) and N the total angular momentum exclusive of spins of the system. It has been discussed in many places (see, in particular, Refs. [33,34,36]) how the rovibronic reaction matrix can be constructed from the clamped-nuclei matrices by means of the frame transformation approach. The building blocks are vibrational integrals of the type

$$\bar{\eta}^{(i)(N,p)}_{\ell v^+ N^+,\ell' v^{+\prime} N^{+\prime}} = \sum_{\Lambda} \langle N^+|\Lambda\rangle^{(\ell,N,p)} \int \chi^{(N^+)}_{v^+}(R)\, \bar{\eta}^{(i)(\Lambda)}_{\ell\ell'}(R) \times \chi^{(N^{+\prime})}_{v^{+\prime}}(R) dR\, \langle\Lambda|N^{+\prime}\rangle^{(\ell',N,p)} \qquad (17)$$

over the clamped-nuclei electronic functions $\bar{\eta}^{(i)}_{\ell\ell'}(R)$ from Eq. (16) as kernels. We add a superscript Λ to these here because the frame transformation expression (17) combines several Λ components together. The frame-transformation expression links the molecule-fixed representation of the wave function to the space-fixed one. The ion ground-state core vibrational wave functions $\chi^{(N^+)}_{v^+}(R)$ play here the role of the vibrational transformation, while the rotational transformation is encoded in the brackets $\langle N^+|\Lambda\rangle^{(\ell,N,p)}$, which are expressed analytically in terms of symmetrized combinations of $3j$ symbols [37].

As a result of the frame transformation the rovibronic reaction matrix has a vastly increased dimension (in principle infinite), which effectively replaces the continuous dependence on R of its clamped-nuclei precursors. We have typically used a basis of 15 ion core vibrational levels v^+ for each value of the rotational quantum number N^+. The sum over Λ in the frame transformation expression (17) runs over $\Lambda = 0$–2 for c-type levels [+ Kronig symmetry with total parity $+(-1)^N$] and over $\Lambda = 1$ and 2 for d-type levels [− Kronig symmetry corresponding to total parity $-(-1)^N$]. In practice, the rovibronic MQDT determinantal system Eq. (13) takes dimensions of the order of 40 to 60 in the present application and involves more than 1000 independent reaction matrix elements. The remarkable power of the frame transformation concept is that all of these are generated from the functions $\bar{\eta}^{(i)(\Lambda)}_{\ell\ell'}(R)$ which are smooth and may be specified by a small number of parameters, as we have seen in the preceding sections.

Smaller effects such as the "normal" and the "specific" mass-dependent contributions to the quantum defect matrices have been included exactly as in the previous paper [19], but are not in the focus here as we consider only one isotopomer in this paper.

B. Input data set and fitting procedure

We have refined the quantum defect functions determined in Sec. IV C by adjusting them to a set of experimental rovibronic levels of triplet gerade H_2. In the spirit of Ref. [19], we included in our least-squares fitting procedure basically the complete set of currently known experimental triplet gerade levels of H_2, extending over a range of nearly 5 eV and including rotational levels of both parities for $0 \leqslant N \leqslant 4$. Information on the $n = 2$ levels stems from Dieke and Crosswhite [38] and from Jungen *et al.* [39], for $n = 3$ from Bailly *et al.* [40], and for $n = 4$ from Eyler and Pipkin [41] and Ross *et al.* [42]. For $n = 2$ and $n = 3$ our data set is more complete than that used in Ref. [19] as we have included the levels $v = 3$–6 of the $2s\sigma a^3\Sigma_g{}^+$ state

and the levels with $v = 3$ of the $3d\ ^3\Sigma_g^+, ^3\Pi_g, ^3\Delta_g$ complex of states which were omitted in the earlier work.

For energies above the $H(1s) + H(n = 2)$ dissociation limit the triplet gerade levels are subject to predissociation, and for energies higher than the $H_2^+(v^+ = 0) + e^-$ threshold they are in addition subject to autoionization; that is, they are broadened by interaction with the dissociation and ionization continua and are, in fact, resonances. Extensive information on these higher Rydberg structures has been gathered by Bjerre *et al.* [43] and Lembo *et al.* [44,45] and most recently by Sprecher *et al.* [19]. Numerous broad predissociation and/or autoioionization resonances corresponding to triplet gerade upper state symmetry with widths Γ/hc up to $\approx 50\ \mathrm{cm}^{-1}$ have been observed in Refs. [43–45], and many of them were later interpreted theoretically in the MQDT study of Matzkin *et al.* [46]. However, for the purpose of the present fit we retain here only the levels listed in Ref. [19] which are "sharp" in the sense that their natural widths are smaller than the experimental resolution width, $\Delta E/hc \approx 0.2\ \mathrm{cm}^{-1}$, achieved in that work. This allows us to treat these levels in our calculations as bound levels, by omitting the open fragmentation continua and by setting the phase parameter β_k for the remaining channels in the determinant Eq. (13) equal to the values appropriate for closed channels given by Eq. (14). In all, we have included 449 experimental rovibronic levels in our least-squares fit.

The least-squares fitting procedure implemented here is similar to that employed in Ref. [19]. The measurements of triplet gerade rovibronic levels reported in Ref. [19] extend from $v^+ = 0$ up near the $v^+ = 4$ H_2^+ vibrational threshold with a gap remaining only between 124 100 and 125 500 cm^{-1}. The $v^+ = 4$ threshold is indicated in Fig. 1, and it may be seen that the classically allowed region for the corresponding ion vibrational level is restricted to $R < 4$ bohr. It is therefore appropriate to fit the functions $\bar{\eta}_{\ell\ell'}^{(i)(\Lambda)}(R)$ in the range $1.4 \leqslant R \leqslant 4$ bohr. As was done previously in Ref. [19], we have determined the corrections to the initial quantum defects rather than the functions themselves. In our case the initial parameters are the R-matrix results obtained in Secs. III and IV, whereas the fitting procedure of Ref. [19] started out from initial quantum defects extracted from the quantum-chemical potential energy curves of Wolniewicz, Kolos, and collaborators [17–21]. While in Ref. [19] it proved sufficient to correct each $\bar{\eta}^{(i)(\Lambda)}$ ($i = 0$–2) from Eq. (16) by a constant plus a linear term in R, we found it necessary to use a larger set of correction terms, of the form

$$\begin{aligned} &c_{\ell\ell'}^{(0)}, \quad c_{\ell\ell'}^{(1)} \sin(\pi x), \quad c_{\ell\ell'}^{(2)}[\cos(\pi x) - 1], \\ &c_{\ell\ell'}^{(3)} \sin(2\pi x), \quad c_{\ell\ell'}^{(4)}[\cos(2\pi x) - 1], \end{aligned} \tag{18}$$

for each value of Λ. Here $x = (R - R_m)/\Delta$, where $R_m = \frac{1}{2}(R_{\mathrm{end}} + R_{\mathrm{beg}})$ and $\Delta = R_{\mathrm{end}} - R_{\mathrm{beg}}$, with R_{beg} and R_{end} the boundaries of the fitting range. The geometric functions in Eq. (18) are chosen in order to avoid unrealistically large correction terms near the boundaries of the fitting range as they would occur in a polynomial expansion.

C. Results and discussion

Table I summarizes the results of the fitting procedure and compares them with the previous fit made in Ref. [19]. Not surprisingly, the initial *ab initio* quantum defect functions derived in the previous paper from quantum-chemical potential energy curves constitute a far better starting point than our initial R-matrix predictions. However, the present fit by and large compensates this drawback, as it produces final root-mean-square deviations that are only about a factor two to three worse than those obtained previously and remain well below $1\ \mathrm{cm}^{-1}$. Our initial predictions of rovibronic levels are seen to be distinctly better for the d-Kronig symmetry levels which are derived uniquely from $^3\Pi_g{}^-$ and $^3\Delta_g{}^-$ Born-Oppenheimer levels than for the full set that includes also the c-Kronig symmetry levels which in addition depend on the $^3\Sigma_g{}^+$ quantum defects. This is a consequence of the fact that, owing to the nonlinear relationship between energies and quantum defects, the largest deviations occur for $n = 2$ where only c levels are present.

More detailed information on the rovibronic calculations is provided by Table II, which lists the deviations observed minus those calculated for a representative subset of $N = 2$ levels with n ranging from 2 to 17 (columns 5 and 8 of the table). The table demonstrates once again that the quantum defects extracted from accurate potential energy curves provide overall a far better starting point than those calculated by our present implementation of R-matrix theory. However, it is also clear that the superiority of the quantum-chemical approach is limited to the lowest n values, essentially $n = 2$ to 4—the region for which quantum-chemical potential curves exist—whereas for higher energies/n values the two approaches become quickly equivalent. It also turns out that some of the

TABLE I. Root-mean-square errors of calculated rovibronic energies from MQDT; Ref. [19] and present work (cm^{-1}).

Symmetry[a]		Number[b]	Range *ab initio*[c]	rms *ab initio*[d]	Range fit	rms fit
d levels	Previous[e]	206	−0.6:2.6	0.73[f]	−0.4:0.4	0.13
	Present	209	−26.5:54.6	12.0[g]	−3.0:0.9	0.40
c and d levels	Previous[e]	419	−5.1:2.3	0.71[f]	−1.2:2.6	0.29
	Present	449	−215.3:57.9	53.2[g]	−3.0:3.2	0.53

[a]Kronig symmetry.
[b]Number of rovibronic levels included in the fit and used in calculating the rms error.
[c]Range of deviations $(E_{\mathrm{obs}} - E_{\mathrm{calc}})/hc$ (cm^{-1}).
[d]Root-mean-square error of initial first-principles calculation (cm^{-1}).
[e]Reference [19].
[f]Quantum defects extracted from potential energy curves of Ref. [17].
[g]Quantum defects calculated with the present R-matrix approach.

TABLE II. Energy deviations observed-calculated for selected $N = 2$ triplet gerade Rydberg levels of H_2 (cm^{-1}).

			Previous[a]		Present		
Parity[b]	Approximate description[c]	Experimental energy[d]	Obs.-calc. initial[e]	Obs.-calc. fit	Obs.-calc. initial[f]	Δn^* initial[f,g]	Obs.-calc. fit
c	$2s\sigma\ a\ ^3\Sigma_g^+, v = 0$	95 275.79	−1.10	0.05	−119.33	−0.0043	−0.07
c	$2s\sigma\ a\ ^3\Sigma_g^+, v = 6$	108 388.55	0.36	2.17	−144.86	−0.0053	0.80
c	$3d\sigma\ g\ ^3\Sigma_g^+, v = 0$	111 826.48	0.23	0.04	−62.44	−0.0077	−0.03
c	$3s\sigma\ h\ ^3\Sigma_g^+, v = 0$	112 049.97	0.01	0.21	−67.01	−0.0082	−0.14
d	$3d\pi\ i\ ^3\Pi_g^-, v = 0$	112 140.80	−0.23	0.05	−16.21	−0.0020	0.04
c	$3d\pi\ i\ ^3\Pi_g^+, v^+ = 0$	112 310.88	0.12	−0.28	−78.76	−0.0097	−0.22
d	$3d\delta\ j\ ^3\Delta_g^-, v = 0$	112 513.90	0.17	−0.19	44.22	0.0054	−0.30
c	$3d\delta\ j\ ^3\Delta_g^+, v = 0$	112 529.55	0.26	−0.08	−3.82	−0.0005	−0.12
c	$4d\sigma\ ^3\Sigma_g^+, v = 0$	117 417.64	−0.61	0.08	−16.24	−0.0006	−0.20
d	$4d\pi\ r\ ^3\Pi_g^-, v = 0$	117 599.44	−0.17	−0.14	8.52	0.0025	−0.52
c	$4s\sigma\ ^3\Sigma_g^+, v = 0$	117 609.61	−0.52	−0.43	−19.75	−0.0058	−0.21
c	$4d\delta\ s\ ^3\Delta_g^+, v = 0$	117 718.98	−0.33	−0.35	−6.42	−0.0019	−0.82
d	$4d\delta\ s\ ^3\Delta_g^-, v = 0$	117 830.35	0.09	0.05	9.35	0.0027	−0.09
c	$4d\pi\ r\ ^3\Pi_g^+, v = 0$	117 958.40	−0.48	0.16	−24.61	−0.0072	0.40
d	$10d\pi, v^+ = 1$	125 561.75	0.79	0.22	−0.43	−0.0020	−0.37
d	$10d\delta, v^+ = 1$	125 576.44	1.45	0.16	0.16	0.0007	0.06
c	$11d0, v^+ = 1$	125 698.83	0.64	0.04	0.07	0.0004	−0.01
c	$6d2, v^+ = 2$	125 760.15	0.20	0.04	−0.82	−0.0008	0.32
c	$11d2, v^+ = 1$	125 864.49	0.31	−0.23	−0.04	−0.0002	0.23
c	$12d2, v^+ = 1$	126 007.72	−0.36	−0.30	−0.02	−0.0002	0.41
c	$17d2, v^+ = 1$	126 434.79	0.02	−0.03	0.21	0.0048	−0.20
d	$6d3, v^+ = 3$	127 799.29	2.06	0.23	−1.27	−0.0012	−0.46
c	$13d2, v^+ = 2$	128 174.56	−0.32	−0.02	−0.21	−0.0021	0.02
d	$11d1, v^+ = 3$	128 417.43	0.73	0.08	−0.89	−0.0054	−0.78
d	$5d\delta, v^+ = 5$	129 922.84	3.77	0.07	8.25	0.0047	−0.24
d	$13d1, v^+ = 4$	131 833.29	1.05	0.19	0.37	0.0037	0.32

[a]Reference [19].
[b]Kronig symmetry: c/d refer to total parity $\pm(-1)^N$, respectively.
[c]Hund's case b Born-Oppenheimer description $n\ell\lambda\ ^3\Lambda_g, v$. Hund's case d description $n\ell N^+, v^+$.
[d]E/hc (cm^{-1}) above $X\ ^1\Sigma_g^+, v = 0, N = 0$.
[e]Quantum defects extracted from *ab initio* potential energy curves.
[f]Quantum defects calculated by *R*-matrix theory.
[g]$\Delta n^* = n^*_{obs} - n^*_{calc}$, error of the effective principal quantum number, with n^* corresponding to the approximate description of the level.

levels for $n = 2$ and 3 which were not included in the fit of Ref. [19] are not too well reproduced by the quantum defects determined there (cf. Table II).

The second-to-last column of Table II lists the errors $\Delta n^* = n^*_{obs} - n^*_{calc}$ of the effective principal quantum numbers as obtained with the initial *R*-matrix quantum defects. These quantities have been evaluated on the basis of the dominating channel component indicated in the second column for each level. Note that they are just the negatives of the effective quantum defects in the sense of Eq. (1). Not surprisingly, the errors Δn^* are seen to be more evenly distributed among the sequence of the selected Rydberg levels than the energy deviations themselves. It turns out that the *ab initio* *R*-matrix approach provides predictions of rovibronic level energies that are correct, on a quantum defect scale, to better than 0.01.

The main final result of the least-squares fitting procedure is a set of adjusted quantum defect functions $\bar{\eta}^{(i)(\Lambda)}_{\ell\ell'}(R)$ ($i = 0$–2). From these the quantum defects $\bar{\eta}_{\ell\ell'}(\epsilon, R)$ can be evaluated by means of Eq. (16) for any arbitrary energy. This is demonstrated in Figs. 9 and 10, where the final functions (orange curves) are confronted with the initial *R*-matrix values (blue circles) for different energies. The comparison of the two sets of curves is gratifying: The adjustments required to bring the observed and predicted rovibronic levels into agreement are minor on the absolute quantum defect scale used in the plots. The most obvious deviation occurs for the $dd\sigma$ channel where the *R*-matrix prediction lies consistently nearly 0.04 lower than the adjusted value. Somewhat surprisingly, this value is considerably larger than all of the deviations Δn^* listed in the second-to-last column of Table II. The reason must be that the observable levels for the most part have mixed character owing to the rovibronic interactions affecting them. Therefore, the quantum defect errors are averaged out to some extent, an effect that is enhanced, no doubt, by the vibrational motion and, as the energy increases, also by the high density of levels which diminishes the energy shifts that can arise from vibronic

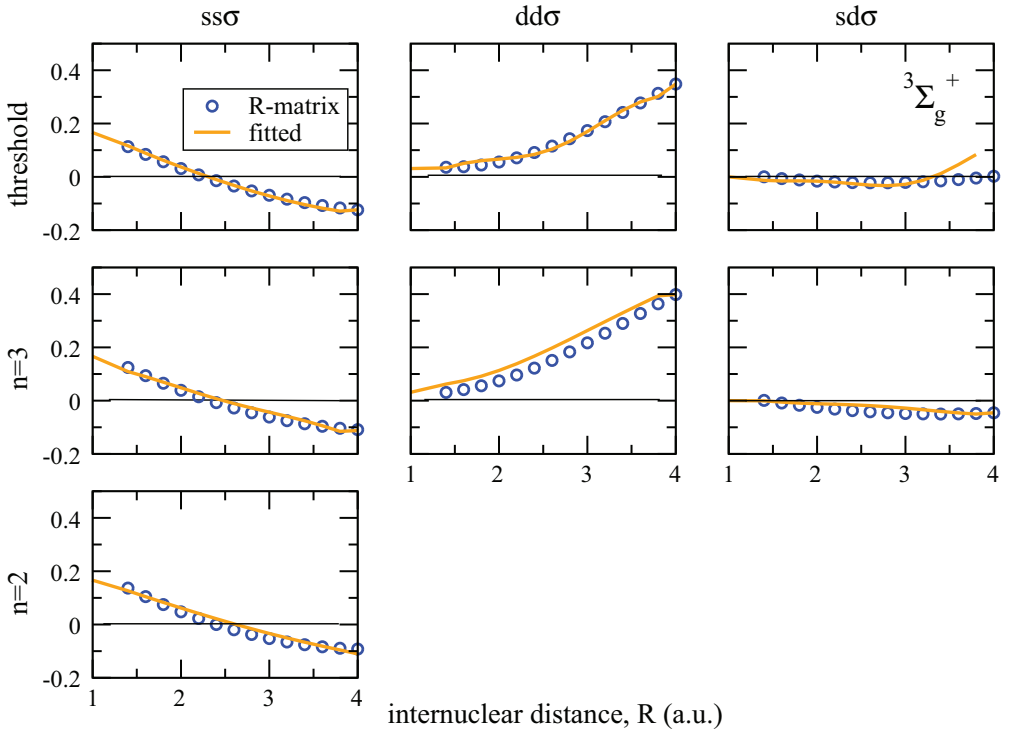

FIG. 9. (Color online) $\bar{\eta}_{ss}$, $\bar{\eta}_{dd}$ $\bar{\eta}_{sd}$ quantum defects for $^3\Sigma_g{}^+$ symmetry channels in H_2 plotted as functions of the internuclear distance R in bohr. (Top row) Values at threshold ($\epsilon = 0$); (middle row) values for $n = 3$ ($\epsilon = -1/9$ Ry); (bottom panel) values for $n = 2$ ($\epsilon = -1/4$ Ry). Circles (blue online), *ab initio* R-matrix values; full lines (orange online), fitted to experiment.

perturbations and/or quantum defect inaccuracies. A smaller systematic deviation occurs for the $dd\delta$ channel where the R-matrix prediction lies 0.02 *higher* than the adjusted value. The $dd\delta$ channel corresponds to a nonpenetrating Rydberg electron and its small quantum defect is determined essentially by the asymptotic field outside the core or reaction zone (quadrupole field and dipole electron-core polarization). The

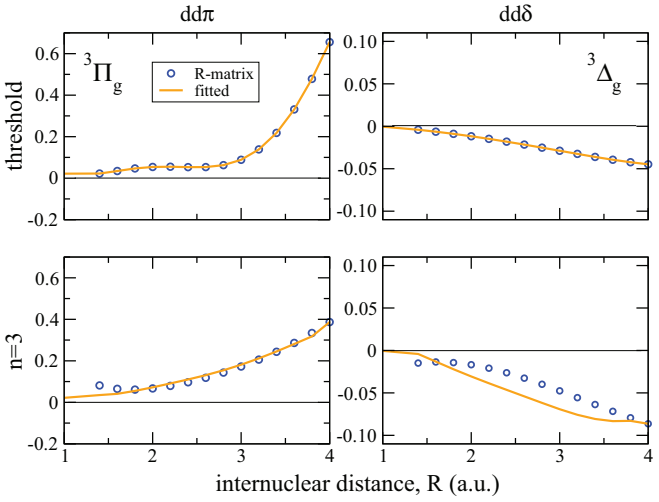

FIG. 10. (Color online) $\bar{\eta}_{dd}$ quantum defects for $^3\Pi_g$ (left column) and $^3\Delta_g$ (right column) symmetry channels in H_2, plotted as functions of the internuclear distance R in bohr. (Top row) Values at threshold ($\epsilon = 0$); (bottom row) values for $n = 3$ ($\epsilon = -1/9$ Ry). Circles (blue online), *ab initio* R-matrix values; full lines (orange online), fitted to experiment.

failure of the R-matrix calculation to account accurately for the quantum defect in this case probably reflects an inadequacy of the asymptotic field used in the halfium approximation; see Sec. III A.

Finally, Table III compares the final clamped-nuclei quantum defect matrix elements $\bar{\eta}^{(\Lambda)}_{\ell\ell'}(\epsilon, R)$ with those determined previously in Ref. [19] on the basis of the same experimental data. The comparison is made for a selected range of R values around the equilibrium internuclear distance of the $H_2{}^+$ core, and values are given for two energies, namely $\epsilon = -1/3^2$ ($n = 3$) and $\epsilon = 0$ ($n = \infty$).

The table shows the following.

(i) For the set of R values chosen the average of the deviations between our values and those of Ref. [19] is about a factor 100 smaller for $n = 3$ than at threshold, and the mean deviation of these differences still is a factor of three smaller for $n = 3$ than for $n = \infty$. This is not surprising because the starting values at threshold were obtained in Ref. [19] by extrapolation from $n = 2$–4 to $n = \infty$, whereas we have calculated them directly with the R-matrix method. It appears likely that our values at threshold are more accurate than the previously determined ones (cf. also Figs. 9 and 10), but in any case a mean deviation <0.01 can be considered as small from the perspective of scattering theory.

(ii) Turning to the comparison for $n = 3$, we see that the average of the deviations ($\approx$0.2 cm^{-1}) is of the order of the quality of the fits obtained here and in the previous paper, which is satisfactory agreement.

(iii) However, the *mean deviation* of the differences is more than two orders of magnitude larger and amounts to 25 cm^{-1}. This mean deviation reflects the erratic occurrence of positive

TABLE III. Previous and present body-frame quantum defects for triplet gerade symmetry in H_2.[a]

		$n = 3$			$n = \infty$ (Threshold)		
Matrix element	R value	$\bar{\eta}$ Previous fit[b]	$\bar{\eta}$ Present fit	Difference	$\bar{\eta}$ Previous fit[b]	$\bar{\eta}$ Present fit	Difference
$ss\sigma$	1.6	0.094 97	0.090 03	−0.004 94	0.084 70	0.088 71	0.004 01
	2.0	0.048 05	0.048 37	0.000 32	0.036 79	0.036 85	0.000 06
	2.4	0.005 90	0.007 47	0.001 57	−0.006 70	−0.010 42	−0.003 72
	2.8	−0.031 38	−0.027 36	0.004 02	−0.045 77	−0.052 69	−0.006 92
	3.2	−0.063 37	−0.058 62	0.004 75	−0.079 97	−0.088 89	−0.008 92
$dd\sigma$	1.6	0.072 49	0.074 80	0.002 31	0.045 30	0.050 60	0.005 30
	2.0	0.113 46	0.113 25	−0.000 21	0.064 04	0.066 60	0.002 56
	2.4	0.166 69	0.166 88	0.000 19	0.092 37	0.084 10	−0.008 27
	2.8	0.230 38	0.230 04	−0.000 34	0.136 25	0.133 07	−0.003 18
	3.2	0.298 67	0.296 45	−0.002 22	0.200 44	0.210 69	0.010 25
$dd\pi$	1.6	0.048 13	0.041 11	−0.007 02	0.026 84	0.034 54	0.007 70
	2.0	0.073 35	0.072 51	−0.000 84	0.040 87	0.053 98	0.013 11
	2.4	0.106 87	0.110 26	0.003 39	0.060 62	0.053 17	−0.007 45
	2.8	0.151 27	0.154 36	0.003 09	0.089 17	0.062 62	−0.026 55
	3.2	0.210 21	0.211 70	0.001 49	0.139 11	0.138 40	−0.000 71
$dd\delta$	1.6	−0.018 06	−0.013 13	0.004 93	−0.007 74	−0.006 40	0.001 34
	2.0	−0.030 53	−0.030 62	−0.000 09	−0.013 17	−0.011 76	0.001 41
	2.4	−0.044 54	−0.046 36	−0.001 82	−0.019 40	−0.018 11	0.001 29
	2.8	−0.059 23	−0.061 75	−0.002 52	−0.026 20	−0.025 19	0.001 01
	3.2	−0.073 68	−0.075 74	−0.002 06	−0.033 47	−0.032 53	0.000 94
$sd\sigma$	1.6	−0.007 35	−0.005 52	0.001 83	−0.001 91	−0.015 28	−0.013 37
	2.0	−0.011 33	−0.011 35	−0.000 02	−0.006 34	−0.016 21	−0.009 87
	2.4	−0.016 21	−0.015 50	0.000 71	−0.011 57	−0.025 53	−0.013 96
	2.8	−0.021 98	−0.022 69	−0.000 71	−0.017 62	−0.033 22	−0.015 60
	3.2	−0.028 65	−0.034 04	−0.005 39	−0.024 47	−0.013 14	0.011 33
Mean difference/ deviation $\bar{\eta}$				0.000 02 ± 0.003 03			−0.002 33 ± 0.009 31
Mean difference/ deviation energy[c]				0.2 ± 24.6 cm^{-1}			

[a]These quantum defects include the mass-dependent contribution of the "specific" mass effect; see [19] for a detailed discussion.
[b]Sprecher *et al.* [19].
[c]Evaluated using the scaling relation $\Delta E = (2\mathcal{R}/3^3)\,\Delta\bar{\eta}$ where $\mathcal{R}$ is the Rydberg constant.

and negative deviations and is probably due to the fact that the correction functions of Eq. (18) are gross approximations to the required corrections. The vibrational motion washes these deviations out and allows nevertheless a good fit of the experimental data to be obtained.

(iv) Once again, however, from the perspective of scattering theory and accuracy of phase shifts the agreement is really excellent, considering that even the largest deviations never exceed a few multiples of 0.001.

VI. CONCLUSION

In this work we have demonstrated how by starting from *ab initio* *R*-matrix calculations, it is possible to produce $e^- \sim H_2^+$ reaction matrices that may be applied to the calculation of high-resolution molecular spectroscopy data on the scale <1 cm^{-1}. While in the bound range, for $n = 2$ and $n = 3$, our initial *R*-matrix quantum defects are less accurate than those extracted from state-of-the-art quantum-chemical potential energy curves by one to two orders of magnitude, they retain their validity at higher energies, far above the ionization threshold where the methods of customary quantum chemistry fail. Figures 9 and 10 show that in units of π radians our *R*-matrix code yields electron-ion scattering phase shifts that are correct to <0.02 in most cases and accurate to 0.05 in all cases, despite the fact that in the *R*-matrix computations reported here we have used minimal angular and radial basis sets. We may thus be confident that this degree of accuracy is maintained in the electronic continuum.

We stress once again that only minor adjustments, which do not alter the overall behavior, have been necessary to bring the initial quantum defect functions into agreement with the high-resolution spectroscopic data from Ref. [19]. Moreover, the initial discrepancies occur almost exclusively for the lowest states, with $n = 2$ and 3 as demonstrated by Table II, where they are due to the highly nonlinear relationship between the quantum defect and the energy. The capability of quantum defect theory—or "multichannel spectroscopy," as it has been called [2]—to provide a global quantitative interpretation of complex experimental data over a considerable energy domain is not invalidated by this fact. Whether a treatment purely from first principles is sufficient or a fit to experimental data

is necessary depends on the accuracy of the experimental data at hand.

In view of the above statements the calculations presented here may be considered as exploratory. It appears desirable to improve future clamped-nuclei R-matrix calculations on all symmetries in H_2 by vastly increasing the basis sets employed. This is technically possible with available computers, and work in this direction is under way. From a conceptual point of view, however, it appears already at this point that a better definition has been achieved of the meaning of quantum defect matrices such as they are extracted empirically from spectroscopic data.

A further planned improvement of our R-matrix approach concerns the refinement beyond the halfium approximation of the field used in the asymptotic zone. Finally, a limitation of the rovibronic MQDT calculations presented here is that they cannot be extended meaningfully beyond the energy range defined by the plots of Figs. 5 and 6, where the reduced clamped-nuclei matrices remain smooth. For higher energies one has to return to the full reaction matrices that explicitly include core-excited channels such as those evaluated in Sec. III B. However, in doing this we wish to preserve the high accuracy attained in the bound range, while recovering the smoothness and generality at higher energy. This extension is deferred to a future publication and will involve "working backward" from the reduced clamped-nuclei quantum defect matrices fitted in Sec. V to the higher-dimension multicore matrices required at higher energy.

ACKNOWLEDGMENTS

Ch. J. was supported in part by the ANR (France) under Contract No. 09-BLAN-020901. H.O. and F.A. have received travel support from the same ANR contract. Ch. J. also received funding from the E. Miescher Foundation (Basel, Switzerland). Further, he is grateful to the ETH (Zürich) and, in particular, to Frédéric Merkt for hospitality during a stay in the Laboratorium für Physikalische Chemie, where he started working on his contribution to the present paper. Finally, Ch. J. acknowledges helpful discussions with Dr. D. Sprecher (ETH Zürich).

[1] P. G. Burke and K. A. Berrington, eds., *Atomic and Molecular Processes: An R-matrix Approach* (Institute of Physics Publishing, Bristol, UK, 1993).
[2] M. Aymar, C. H. Greene, and E. Luc-Koenig, Rev. Mod. Phys. **68**, 1015 (1996).
[3] J. Tennyson, Phys. Rep. **491**, 29 (2010).
[4] G. Raseev and H. Le Rouzo, Phys. Rev. A **27**, 268 (1983).
[5] J. Tennyson, C. J. Noble, and S. Salvini, J. Phys. B: At. Mol. Opt. Phys. **17**, 905 (1984).
[6] G. Raseev, J. Phys. B **18**, 423 (1985).
[7] J. Tennyson and C. J. Noble, J. Phys. B: At. Mol. Opt. Phys. **18**, 155 (1985).
[8] J. Tennyson, J. Phys. B: At. Mol. Opt. Phys. **21**, 805 (1988).
[9] I. Shimamura, C. J. Noble, and P. G. Burke, Phys. Rev. A **41**, 3545 (1990).
[10] B. K. Sarpal, S. E. Branchett, J. Tennyson, and L. A. Morgan, J. Phys. B: At. Mol. Opt. Phys. **24**, 3685 (1991).
[11] C. H. Greene and B. Yoo, J. Phys. Chem. **99**, 1711 (1995).
[12] I. Rabadan and J. Tennyson, J. Phys. B: At. Mol. Opt. Phys. **29**, 3747 (1996); **30**, 1975 (1997).
[13] M. Arif, Ch. Jungen, and A. L. Roche, J. Chem. Phys. **106**, 4102 (1997).
[14] M. Hiyama and M. S. Child, J. Phys. B: At. Mol. Opt. Phys. **35**, 1337 (2002).
[15] M. Telmini and Ch. Jungen, Phys. Rev. A **68**, 062704 (2003).
[16] S. Bezzaouia, M. Telmini, and Ch. Jungen, Phys. Rev. A **70**, 012713 (2004).
[17] http://fizyka.umk.pl/ftp/pub/publications/ifiz/luwo.
[18] See, e.g., the compilation of references given in M. Glass-Maujean, Ch. Jungen, H. Schmoranzer, I. Tulin, A. Knie, P. Reiss, and A. Ehresmann, J. Mol. Spectrosc. **293**, 19 (2013).
[19] D. Sprecher, Ch. Jungen, and F. Merkt, J. Phys. Chem. A **117**, 9462 (2013).
[20] G. Staszewska and L. Wolniewicz, J. Mol. Spectrosc. **198**, 416 (1999).
[21] W. Kolos and J. Rychlewski, J. Mol. Spectrosc. **177**, 146 (1996).
[22] G. Herzberg, *Molecular Spectra and Molecular Structure. I. Spectra of Diatomic Molecules*, 2nd ed. (Krieger, Malabar, FL, 1989).
[23] R. S. Mulliken, J. Am. Chem. Soc. **91**, 4615 (1969).
[24] J. A. Stephens and V. McKoy, J. Chem. Phys. **97**, 8060 (1992).
[25] R. S. Mulliken, J. Am. Chem. Soc. **88**, 1849 (1966).
[26] C. H. Greene, Phys. Rev. A **28**, 2209 (1983).
[27] Ch. Jungen and F. Texier, J. Phys. B: At. Mol. Opt. Phys. **33**, 2495 (2000).
[28] H. Oueslati, M. Telmini, and Ch. Jungen, Mol. Phys. **104**, 187 (2006).
[29] F. Argoubi, S. Bezzaouia, H. Oueslati, M. Telmini, and Ch. Jungen, Phys. Rev. A **83**, 052504 (2011).
[30] S. Bezzaouia, F. Argoubi, M. Telmini, and Ch. Jungen, J. Phys. Conf. Ser. **300**, 012013 (2011).
[31] S. Bezzaouia and M. Telmini, AIP Conf. Proc. **935**, 183 (2007).
[32] M. J. Seaton, Rep. Prog. Phys. **46**, 167 (1983).
[33] C. H. Greene and Ch. Jungen, Adv. At. Mol. Phys. **21**, 51 (1985).
[34] Ch. Jungen, in *Handbook of High-resolution Spectroscopy*, edited by M. Quack and F. Merkt (Wiley & Sons, New York, 2011), p. 471.
[35] R. W. Field, C. M. Gittins, N. A. Harris, and Ch. Jungen, J. Chem. Phys. **122**, 184314 (2005).
[36] S. C. Ross and Ch. Jungen, Phys. Rev. A **49**, 4364 (1994).
[37] Ch. Jungen and G. Raseev, Phys. Rev. A **57**, 2407 (1998).
[38] H. M. Crosswhite, *The Hydrogen Molecule Wavelength Tables of Gerhard Heinrich Dieke* (Wiley-Interscience, New York, 1972).
[39] Ch. Jungen, I. Dabrowski, G. Herzberg, and M. Vervloet, J. Chem. Phys. **93**, 2289 (1990).
[40] D. Bailly and M. Vervloet, Mol. Phys. **105**, 1559 (2007).

[41] E. E. Eyler and F. M. Pipkin, Phys. Rev. A **27**, 2462 (1983).
[42] S. C. Ross, Ch. Jungen, and A. Matzkin, Can. J. Phys. **79**, 561 (2001).
[43] N. Bjerre, S. R. Keiding, L. J. Lembo, and H. Helm, Phys. Rev. Lett. **60**, 2465 (1988).
[44] L. J. Lembo, D. L. Huestis, S. R. Keiding, N. Bjerre, and H. Helm, Phys. Rev. A **38**, 3447 (1988).
[45] L. J. Lembo, N. Bjerre, D. L. Huestis, and H. Helm, J. Chem. Phys. **92**, 2219 (1990).
[46] A. Matzkin, Ch. Jungen, and S. C. Ross, Phys. Rev. A **62**, 062511 (2000).